

# Comparative study of one-step and two-step quantitative fluorescence photoacoustic tomography

PRABODH KUMAR PANDEY,<sup>1</sup>  OMPRAKASH GOTTAM,<sup>2</sup>  NAREN NAIK,<sup>2,3,\*</sup>  AND ASIMA PRADHAN<sup>1,3</sup> 

<sup>1</sup>Department of Physics, Indian Institute of Technology, Kanpur 208016, India

<sup>2</sup>Department of Electrical Engineering, Indian Institute of Technology, Kanpur 208016, India

<sup>3</sup>Centre for Laser and Photonics, Indian Institute of Technology, Kanpur 208016, India

\*Corresponding author: [nnaik@iitk.ac.in](mailto:nnaik@iitk.ac.in)

Received 20 November 2018; revised 5 March 2019; accepted 15 March 2019; posted 18 March 2019 (Doc. ID 352460); published 15 April 2019

Fluorescence optical tomography (FOT) is a well-known imaging technique, where fluorescent biological markers are injected to tag targeted tissues (tumors, proteins), and the absorption coefficient of fluorophore is reconstructed to provide contrast-enhanced images. Conventional FOT is known to have lack of stability to noise and shallow imaging depth due to strong optical scattering in biological tissue. Photoacoustic tomography (PAT) has been previously proposed to combine with FOT to resolve this issue. We propose a fully nonlinear one-step reconstruction in a diffuse-approximation modeled fluorescence photoacoustic tomographic (FPAT) setting, where the absorption coefficient of exogenous fluorophore is recovered directly from the photoacoustic data. Computational validations in two dimensions in single- and dual-grid reconstruction settings using full as well as partial data have been provided in support of the proposed algorithm. One-step schemes are particularly useful with respect to dual representations of field (optical and pressure) variables and optical parameters, especially in limited-data settings, which effectively help in constraining the optimization search space. We have compared the results of one- and two-step FPAT schemes and concluded that the one-step reconstructions are superior as compared with the corresponding two-step reconstructions. To the best of our knowledge, these are the first comparisons of one-step and two-step reconstructions in FPAT. © 2019 Optical Society of America

<https://doi.org/10.1364/AO.58.003116>

## 1. INTRODUCTION

Biological/biochemical changes in the human body are accompanied by changes in local absorption and scattering properties of tissue. Diffuse optical tomography (DOT) is a well explored noninvasive biomedical imaging technique that aims to recover the distribution of optical absorption and scattering properties of tissue. One of the most important applications of DOT is tumor detection in soft tissues. Tumor development is followed by higher blood flow to local tissues and hence leads to changes in absorption properties of the tissue. However, at the earlier stages of tumor development, this absorption contrast is not significant enough to provide good sensitivity and specificity in tumor detection [1]. To improve this contrast, fluorescent markers are injected to tag the targeted tissues (tumors), and spatial distribution of exogenous fluorophore concentration is reconstructed using fluorescence optical tomography (FOT) [1,2]. Fluorescent markers have been widely employed to enhance the PA signals and hence assist in deep photoacoustic (PA) imaging [3,4]. Fluorescent markers having high quantum efficiencies while having low toxicity are reported to be under

development [5]. Major progress has been made in disease-specific fluorescent markers, experimental setups, and reconstruction algorithms of FOT [6,7].

Consequently, the quality of images produced by FOT has improved very much, but the major issue that still remains is its lack of stability due to light getting multiply scattered in the turbid media [2,8,9]. Various algorithmic as well as experimental approaches have been proposed in order to resolve the issue. The seminal paper of Ren and Zhao (2013) proposed the assistance of photoacoustic tomography (PAT) to stabilize the FOT reconstructions by reconstructing the optical parameters from photoacoustically reconstructed absorbed optical energy density (AOED), thus yielding fluorescence photoacoustic tomography (FPAT) [10]. They have proved the uniqueness and stability properties of this inversion problem and shown the reconstructions using AOED as data. The group further developed the theory for radiative transport equation (RTE) based FPAT and validated it using numerical simulations [11]. Recently, Wang and Zhou (2018) proposed an approach that combines a squeeze iterative method (SIM) with a nonlinear

optimization technique to enhance the quantitative accuracy and convergence of RTE-based FPAT reconstructions [12].

In 2007, Razansky and Ntziachristos reported a hybrid photoacoustic fluorescence molecular tomography (PA-FMT), which uses a PA reconstruction to generate an approximate absorption coefficient distribution to improve FMT reconstruction quality [13]. The universal backprojection (UBP) technique was utilized to reconstruct the AOED map of the phantom from PA measurements. The AOED map was further normalized by an analytically calculated diffusion-approximated optical fluence map for a phantom with constant and known absorption properties, and a quantitative map of absorption coefficient was approximated. The chromophore absorption map thus obtained was used to solve the linear FMT reconstruction problem for the fluorophore absorption coefficient.

PAT has already been combined with DOT (known as quantitative photoacoustic tomography [QPAT]) to produce highly accurate absorption as well as a scattering coefficient map of endogenous chromophores [14–21]. A typical QPAT is a two-step process: the AOED is reconstructed from the boundary PA measurements in the first step, and the second step recovers the maps of optical parameters from the photoacoustically reconstructed AOED map. The two-step QPAT has been studied in detail by several groups around the globe [14–19]. In 2012, Yuan and Jiang presented a one-step algorithm to accurately recover the optical absorption coefficient from multifrequency boundary PA data. The reconstructions thus obtained were reported to be improved as compared with the two-step reconstructions [20]. An iterative stochastic filtering algorithm had been proposed in [22] for direct recovery of the absorption coefficient map from multifrequency boundary PA measurements. In 2016, Venugopal *et al.* presented a stochastic approach to one-step QPAT from time-domain PA data [21] and reported its superiority over the two-step QPAT.

We note that a one-step scheme is particularly useful in dual-representation (of field [optical and acoustic] variables and optical parameters) methods especially needed in limited-data settings because they effectively constrain the optimization search space. In [23], preliminary studies on a one-step FPAT scheme were reported to recover the fluorophore absorption coefficient from boundary PA measurements. The contribution of the present work is a detailed computational study of one-step schemes and comparison with two-step schemes in a Tikhonov regularized reconstruction framework for diffusion approximated FPAT. Reconstructions have been carried out in single- and dual-grid representations and for complete as well as limited data settings with tissue-mimicking phantoms for data of varying noise levels. To the best of our knowledge, these are the first comparisons of one- and two-step reconstructions in FPAT.

FPAT differs from QPAT in the fact that the initial heat source as well as the measured PA signals also have contributions from the fluorescence light. The partial optical inverse problem of reconstructing an unknown fluorophore absorption coefficient under diffusion approximation assuming a known pressure source has been discussed in [10]. The corresponding RTE-based FPAT problem has been solved in [11,12]. The inverse problem of FPAT can be formulated in two ways:

(1) **Two-step algorithm:** The AOED is first reconstructed from the pressure signal at the detector grid using PAT followed by recovery of fluorophore concentration considering the PA reconstruction as the data. In [10], the second step has been formulated and validated by Ren and Zhao. The authors reconstructed the fluorophore absorption coefficient and the quantum efficiency from two sets of noiseless as well as noisy synthetic internal data sets. However, it needs to be noted that the errors in the PAT reconstructions occur because of errors inherent to the reconstruction algorithms and data insufficiency. The nature of such reconstruction errors is naturally different from what one would have if one only incorporates random multiplicative noise. In this paper, we have shown the reconstructions obtained by solving the complete two-step FPAT inverse problem.

(2) **One-step algorithm:** Reconstruction of fluorophore absorption coefficient is computed directly from the pressure signal at the detector grid. Preliminary results of this algorithm have been reported in our previous work [23]. We solve the fully nonlinear reconstruction problem with the FOT process being modelled by the steady-state coupled photon diffusion equation and the acoustic part by the Helmholtz equation with a heat-source (AOED) term.

In the rest of this paper, Section 2 contains the forward mathematical model of FPAT with its corresponding finite element formulation, defines the reconstruction problem of interest, and motivates the need to use an FPAT formulation over a QPAT one. In Section 3, we set up reconstruction schemes for one- and two-step algorithms in single- as well as dual-grid frameworks. In Section 4, numerical validations are provided in support of the proposed algorithms, and the reconstruction results are discussed in Section 5. Concluding remarks are presented in Section 6.

## 2. PROBLEM DEFINITION AND MOTIVATION

A hybrid photoacoustic-optical (PA-optical) tomographic problem aims to recover the map of optical parameters (e.g., absorption and scattering coefficients, fluorophore concentration, anisotropy factor, etc.) in the region of interest from the measured PA pressure data. The coupled PA-optical forward problem is solved to predict the PA measurements at multiple detector positions. The inverse problem addresses the recovery of desired optical parameters' maps from the PA pressure signal measurements.

### A. Forward Model

#### 1. Fluorescent Light Propagation

Photon transport in turbid media is governed by the radiative transport equation (RTE) [24]. Under the diffusion approximation for scattering-dominant media, the RTE reduces to the diffusion equation. The propagation of excitation light (wavelength  $\lambda_x$ ) along with generation and propagation of fluorescence light (wavelength  $\lambda_m$ ), in the domain  $\Omega_d \subset R^d$  ( $d = 2$  or 3) with boundary  $\partial\Omega_d$ , is commonly modeled in the steady-state by the coupled diffusion equations (CDE) [25] as

$$\begin{aligned} -\nabla \cdot (D_x \nabla \Phi_x) + k_x \Phi_x &= S_x \\ -\nabla \cdot (D_m \nabla \Phi_m) + k_m \Phi_m &= \beta \Phi_x \quad \text{in } \Omega_d, \end{aligned} \quad (1)$$

subject to the Robin boundary conditions

$$\vec{n} \cdot (D_{x/m} \nabla \Phi_{x/m}) + b_{x/m} \Phi_{x/m} = 0 \quad \text{on } \partial\Omega_d, \quad (2)$$

with  $D_{x/m} = \frac{1}{3(\mu_{a(x/m)i} + \mu_{a(x/m)f} + \mu'_{s(x/m)})}$ ,  $k_{x/m} = \mu_{a(x/m)i} + \mu_{a(x/m)f}$ ,  $\beta = \phi \mu_{axf}$ ,  $b_{x/m} = \frac{1-R_{x/m}}{2(1+R_{x/m})}$ . The quantities with subscripts  $x$  and  $m$  correspond to their values at excitation and emission wavelengths, respectively.  $\nabla$  is the  $2 \times 1$  gradient operator,  $\vec{n}$  is the  $2 \times 1$  vector normal to the boundary,  $S_x$  is intensity source,  $\Phi_x$  is the excitation fluence,  $\Phi_m$  is the emission fluence,  $D_{x,m}$  are diffusion constants at excitation and emission wavelengths, respectively, and, similarly,  $k_{x,m}$  are decay coefficients,  $(\mu_{axi}, \mu_{ami})$  are absorption coefficients due to nonfluorescing chromophore,  $(\mu_{axf}, \mu_{amf})$  are absorption coefficients due to exogenous markers, and  $(\mu'_{sx}, \mu'_{sm})$  are reduced scattering coefficients, (all in  $\text{cm}^{-1}$ ) at the two wavelengths.  $\beta$  is the emission source coefficient,  $\phi$  is fluorescence quantum efficiency,  $(b_x, b_m)$  are the Robin boundary coefficients, and  $(R_x, R_m)$  are the Fresnel reflection coefficients. The fluorophore absorption coefficient (at excitation wavelength  $\lambda_x$ )  $\mu_{axf}$  is directly proportional to the fluorophore concentration  $C$ , i.e.,  $\mu_{axf}(\vec{r}) = \epsilon C(\vec{r})$ , where  $\epsilon$  is the molar extinction coefficient at excitation wavelength. We will thus use the fluorophore absorption coefficient ( $\mu_{axf}$ ) instead of the fluorophore concentration  $C$ .

## 2. Photoacoustic Modeling

The total AOED  $h(\vec{r})$  at a location  $\vec{r}$  is given by

$$h(\vec{r}) = k_x(\vec{r})\Phi_x(\vec{r}) + k_m(\vec{r})\Phi_m(\vec{r}). \quad (3)$$

The medium is heated up due to the absorbed optical energy and undergoes thermoelastic expansion to produce a pressure (PA) field inside the medium. In practice, the time scale of light propagation as well as the pulse width of excitation light is much smaller than the time scale of acoustic propagation; thus, the electromagnetic excitation can be approximated as delta pulse excitation. The propagation of PA waves due to delta pulse excitation in acoustically homogeneous nonabsorbing media is governed by the PA equation [26]. The PA equation in the frequency domain can be written as [27]

$$(\nabla^2 + k^2)p(\vec{r}, k) = ik \frac{v\beta}{C_p} h(\vec{r}), \quad (4)$$

with absorbing boundary condition (ABC) [28]

$$\vec{n} \cdot \nabla p(\vec{r}) + ikp(\vec{r}) = 0 \quad \text{on } \partial\Omega_p, \quad (5)$$

where  $h(\vec{r})$  is AOED as defined in Eq. (3),  $k$  is the acoustic wavenumber,  $v$  is the speed of sound,  $\beta$  is the volumetric expansion coefficient, and  $C_p$  is the specific heat at constant pressure. The boundary condition above is a second-order ABC to avoid artificial reflections from the computational domain boundary, derived in [29], which reduces to Eq. (5) for rectangular domains. The discrete-domain equation for PA measurements at detector positions  $\vec{r}_{d_i}$  ( $i = 1, \dots, M$ ) and frequencies  $\omega_j$  ( $j = 1, \dots, L$ ) is formally expressed as

$$\underline{p}_{\text{meas}} \equiv \mathcal{G}(\underline{\mu}_{axf}), \quad (6)$$

where  $\mathcal{G}$  is the discrete-domain measurement operator explicitly given in Eq. (C4) of Appendix C, and  $\underline{p}_{\text{meas}}$  and  $\underline{\mu}_{axf}$  are the

concatenated vectors corresponding to the measured pressure signal and discrete fluorophore absorption coefficient distribution, respectively.

## B. Inverse Problem

The FPAT inverse problem is to reconstruct from a set of PA measurements the spatial distributions of the underlying optical parameters  $\mu_{axi}, \mu_{ami}, \mu'_{sx}, \mu'_{sm}, \mu_{axf}$  that produced them, i.e., the unknown parameters in the map:

$$\Lambda_{\mu_{axi}, \mu_{ami}, \mu'_{sx}, \mu'_{sm}, \mu_{axf}} : S_x(\vec{r}) \mapsto p_{\text{meas}}(\vec{r}_d, \omega)_{|\{\vec{r}_{d_1} \dots \vec{r}_{d_M}\} \times \{\omega_1 \dots \omega_L\}}, \quad (7)$$

where  $\vec{r}_{d_i}$  ( $i = 1, \dots, M$ ) and  $\omega_j$  ( $j = 1 \dots L$ ) denote the position vector of the  $i$ th detector and  $j$ th frequency of the PA measurement.

The recovery of  $\mu_{axi}$  and  $\mu'_{sx}$  can be carried out using QPAT [14,20] at excitation wavelength, before injecting the markers. Similarly, the recovery of  $\mu_{ami}$  and  $\mu'_{sm}$  can be carried out using QPAT at the emission wavelength. When biological markers are injected into the tissue-like medium, they get tagged with the cancerous tissues and fluoresce on excitation. Recovery of the sources of fluorescent emissions, i.e., the spatial concentration map or the absorption coefficient map  $\mu_{axf}(\vec{r})$  of the markers reveal the size and location of tumors inside the tissue; this is the focus in the current work and is described in the sequel.

## C. Motivation for FPAT

Many practical applications utilize biochemical markers, which have low quantum efficiency  $\phi$ . In such cases, the contribution of fluorescence [second term of Eq. (3)] to the photoacoustic heat source becomes negligible; therefore, the FPAT problem practically becomes a QPAT problem. However, when the quantum efficiency is significantly greater than zero, the contribution of the fluorescence heat term in Eq. (3) becomes significant and, neglecting that, in the reconstructions yields erroneous results. We note that, of late, fluorescent markers having high quantum efficiencies while having low toxicity are reported to be under development [5].

To motivate the use of the FPAT formulation rather than only QPAT, we have demonstrated reconstructions of the absorption coefficient at excitation frequency ( $\mu_{axf}$ ) from a noiseless heat source corresponding to a test phantom, i.e., only the second-step reconstructions are carried out here from the accurately generated heat source from a ground truth. The test phantom was chosen to have homogeneous fluorescence distribution in the domain ( $\mu_{axf} = 0.005 \text{ cm}^{-1}$ ) and three circular fluorescent targets ( $\mu_{axf} = 0.04, 0.045$ , and  $0.05 \text{ cm}^{-1}$ );  $\mu_{amf} = 0.1012 \cdot \mu_{axf}$  (as in [30,31]). Significant quantum efficiencies ( $\phi = 0.2, 0.4, 0.6$ ) were chosen for comparison of the FPAT and QPAT frameworks. Such ranges of values are also used in [10–12,32].

As we increased the quantum efficiency  $\phi$ , we observed significant improvements using the FPAT framework rather than only the QPAT. Figure 1 shows the  $\mu_{axf}$  reconstructions when the contribution of fluorescence to the heat source is considered (FPAT reconstruction) or neglected (QPAT reconstruction). The reconstructions have also been quantified in Table 1 in terms of the error measures *correlation coefficient* ( $\rho$ ) and

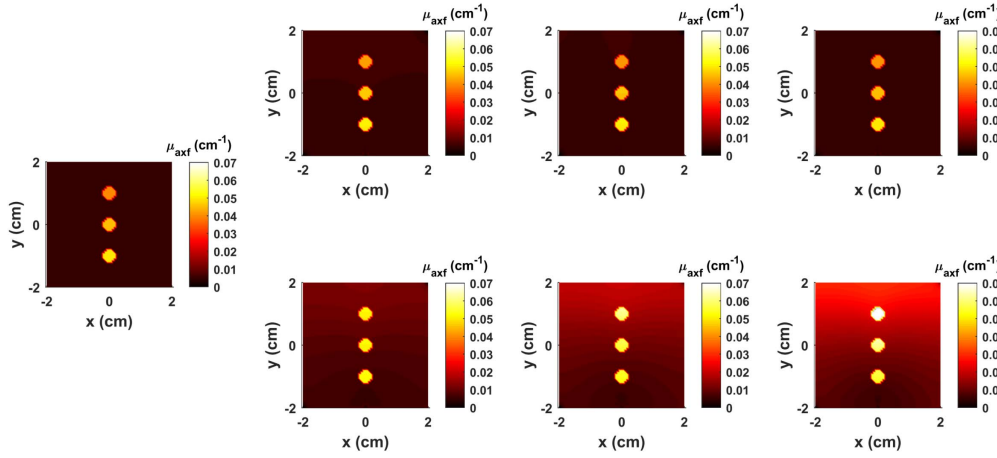


**Fig. 1.** Reconstructions of optical parameters from noiseless heat source generated from a ground truth. Leftmost is the actual phantom; top and bottom rows correspond to second step FPAT and QPAT reconstructions, respectively; columnwise, left to right correspond to quantum efficiency  $\phi = 0.2, 0.4$  and  $0.6$ , respectively.

**Table 1. Error Measures for the Second-Step Reconstructions Based on FPAT and QPAT Frameworks**

Method	$\phi = 0.2$		$\phi = 0.4$		$\phi = 0.6$	
	$\rho$	$\delta$	$\rho$	$\delta$	$\rho$	$\delta$
FPAT	0.99	0.08	0.99	0.06	0.99	0.08
QPAT	0.95	0.65	0.84	1.29	0.70	2.10

deviation factor ( $\delta$ ) [33] (definitions given in this paper in Section 5). In the present work, we carry out numerical studies for phantoms with  $\phi = 0.4$ .

### 3. RECONSTRUCTION SCHEMES

With the markers injected, the tissue is excited by an optical pulse at excitation wavelength ( $\lambda_x$ ), and the PA measurements  $p_{\text{meas}}(\vec{r}_d, \{\omega_i\})$  are obtained. Experimentally, the frequency-domain PA data are generated by taking the Fourier transform of the time-domain PA measurements. After recording the PA data, we need to recover the map of exogenous fluorophore absorption coefficient  $\mu_{\text{axf}}(\vec{r})$  in the tissue. As mentioned in Section 1, it can be carried out using two schemes.

#### A. Two-Step Algorithm

The two-step FPAT reconstruction algorithm involves the recovery of the initial PA source  $p_0(\vec{r})$  and hence the AOED  $h(\vec{r})$  from the PA measurements  $p_{\text{meas}}(\vec{r}_d, \{\omega_i\})$  using PAT in the first step; then, the fluorophore absorption coefficient  $\mu_{\text{axf}}(\vec{r})$  is reconstructed considering the reconstructed AOED as the internal data. In the first step, we aim to solve the following least-squares (LS) problem:

$$\hat{\underline{h}} = \arg \min_{\underline{h}} \epsilon_1(\underline{h}) = \|\underline{p}_{\text{meas}} - \underline{J}_b \underline{h}\|_2^2, \quad (8)$$

where  $\underline{h}$  is the vector of the nodal values of the AOED ( $h(\vec{r})$ ), and  $\underline{J}_b$  denotes the PA measurement matrix. The formation of  $\underline{J}_b$  [27] is given in Eq. (C2) of Appendix C.  $\underline{p}_{\text{meas}} = (p_{\text{meas}}^{1,1}, \dots, p_{\text{meas}}^{M,1}, p_{\text{meas}}^{1,2}, \dots, p_{\text{meas}}^{M,2}, \dots, p_{\text{meas}}^{1,L}, \dots, p_{\text{meas}}^{M,L})^T$  is the measured

PA data and  $\|\cdot\|_2$  denotes the appropriate  $L^2$ -norm. The present problem being ill-posed [27], we solve the corresponding Tikhonov regularized LS problem:

$$\hat{\underline{h}} = \arg \min_{\underline{h}} \epsilon_1(\underline{h}) = \|\underline{p}_{\text{meas}} - \underline{J}_b \underline{h}\|_2^2 + \lambda^2 \|\underline{h}\|_2^2, \quad (9)$$

where  $\lambda$  denotes the regularization parameter. This functional can be straightforwardly solved to obtain the reconstructed  $\underline{h}$  as

$$\hat{\underline{h}} = (\underline{J}_b^T \underline{J}_b + \lambda^2 \mathbf{I})^{-1} \underline{J}_b^T \underline{p}_{\text{meas}}. \quad (10)$$

The regularization parameter  $\lambda$  can be determined using regularization schemes [34]; in our work, we use the L-curve method.

Once the map of discrete domain AOED in the medium is reconstructed ( $\hat{\underline{h}}$ ), we need to solve the following nonlinear LS problem in order to recover the fluorophore absorption coefficient map of exogenous markers ( $\mu_{\text{axf}}$ ) considering  $\hat{\underline{h}}$  as the measured internal data:

$$\hat{\underline{\mu}}_{\text{axf}} = \arg \min_{\underline{\mu}_{\text{axf}}} \epsilon_2(\underline{\mu}_{\text{axf}}) = \|\hat{\underline{h}} - b(\underline{\mu}_{\text{axf}})\|_2^2, \quad (11)$$

where  $\underline{\mu}_{\text{axf}}$  is the vector containing the nodal values of fluorophore absorption coefficient distribution  $\mu_{\text{axf}}$ ,  $b(\underline{\mu}_{\text{axf}})$  is the predicted AOED map for a nominal fluorophore absorption coefficient distribution. We have used a Gauss-Newton scheme to solve this LS problem, and the GN update  $\Delta \underline{\mu}_{\text{axf}}$  is computed using

$$\Delta \underline{\mu}_{\text{axf}} = (\underline{J}_\mu^T \underline{J}_\mu)^{-1} \underline{J}_\mu^T (\hat{\underline{h}} - b(\underline{\mu}_{\text{axf}})), \quad (12)$$

and the updated parameter is obtained as

$$\underline{\mu}_{\text{axf}} := \underline{\mu}_{\text{axf}} + \alpha \Delta \underline{\mu}_{\text{axf}}, \quad (13)$$

where  $\alpha$  is the step-length computed by line search [35]. This inverse problem is quite similar to that of FOT, apart from the fact that, in standard FOT, the value of fluence ( $\Phi_x, \Phi_m$ ) is known only at points on the boundary, while here we have the distribution of AOED ( $h(\vec{r}) = k_x \Phi_x + k_m \Phi_m$ ) throughout



the domain. The elements of Jacobian  $[J_\mu]_{N \times N}$  for this problem are calculated as  $\frac{\partial h_i}{\partial \mu_{axf_j}}$  (change in the  $h$  value at the  $i$ th node, due to perturbation in the parameter  $\mu_{axf}$  at  $j$ th node) and obtained as

$$\begin{aligned} J_{\mu_{ij}} &= \frac{\partial h_i}{\partial \mu_{axf_j}} = k_{x_i} \frac{\partial \Phi_{x_i}}{\partial \mu_{axf_j}} + \Phi_{x_i} \frac{\partial k_{x_i}}{\partial \mu_{axf_j}} \\ &\quad + k_{m_i} \frac{\partial \Phi_{m_i}}{\partial \mu_{axf_j}} + \Phi_{m_i} \frac{\partial k_{m_i}}{\partial \mu_{axf_j}} \\ &= k_{x_i} J_{x_{ij}} + \Phi_{x_i} \delta_{ij} + k_{m_i} J_{m_{ij}} + \gamma \Phi_{m_i} \delta_{ij}, \end{aligned} \quad (14)$$

where  $\gamma = \mu_{amf}/\mu_{axf}$  is the ratio of the absorption coefficients of the exogenous fluorophores at emission and excitation wavelengths,  $J_x$  and  $J_m$  are the standard FOT Jacobians for excitation and emission data, considering all  $N$  nodes in the domain as detectors. The FOT Jacobians  $J_x$  and  $J_m$  have been constructed using adjoint sensitivity calculations carried out in [25].

### B. One-Step Algorithm

In this algorithm, we propose to recover the fluorophore absorption coefficient  $\mu_{axf}$  directly from the forward PA measurements by solving the following nonlinear LS problem:

$$\hat{\mu}_{axf} = \arg \min_{\mu_{axf}} e_3(\mu_{axf}) = \|\underline{p}_{\text{meas}} - \mathcal{G}(\mu_{axf})\|^2. \quad (15)$$

We use the Levenberg–Marquardt (LM) scheme to solve this minimization problem, and the updated iterates are given as in Eq. (13), with the step  $\Delta \mu_{axf}$  being given as

$$\Delta \mu_{axf} = (J^T J + \kappa^2 \mathbf{I})^{-1} J^T (\underline{p}_{\text{meas}} - \mathcal{G}(\mu_{axf})), \quad (16)$$

where  $J$  is the Jacobian for the one-step algorithm and is defined as the variation in  $\underline{p}_{\text{meas}}$  value at the  $i$ th detector node, due to a variation in the parameter  $\mu_{axf}$  at the  $j$ th image node and is constructed as

$$J = J_h J_\mu. \quad (17)$$

The damping parameter  $\kappa$  is computed from the L-curve method.

### C. Dual-Grid Reconstruction Scheme

The optical and pressure field values vary rapidly in the domain. Consequently, an appropriate high-resolution meshing is imperative for accurate forward modeling. However, the optical parameters do not vary as rapidly in the domain, thus allowing for a coarse meshing to represent them. Hence, a so-called dual-grid reconstruction [36,37] employs a suitably coarse-grid representation of the optical parameter  $\mu_{axf}$  in our case. The dual-grid scheme is implemented in a regularized LS framework via the following steps: (i) interpolating the optical parameter from a coarse-grid to a fine-grid and computing the forward solution, and (ii) calculating the Jacobian to update the nodal values of the optical parameter on the coarse-grid. The fine meshing in this work is done by splitting each of the coarse elements into four fine elements (as depicted in Fig. 2).

The value of a parameter  $q$  at  $i$ th node of the fine mesh can be expressed in terms of the nodal values of the coarse mesh as

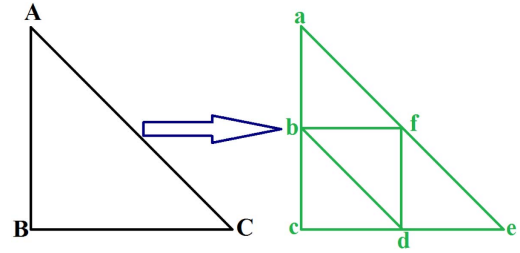


**Fig. 2.** Splitting a coarse element (ABC) into four fine elements (abf, bcd, bdf, and fde).

$$q_{f_i} = \sum_{j=1}^{N_c} \xi_{ij} q_{c_j}, \quad (18)$$

where  $q_{f_i}$  and  $q_{c_j}$  are the values of the parameter  $q$  at  $i$ th node of the fine mesh and at  $j$ th node of the coarse mesh, respectively, and  $N_c$  is the number of nodes in the coarse mesh. In compact notation, we can write Eq. (18) as

$$\underline{q}_f = \Xi \underline{q}_c, \quad (19)$$

where  $\Xi$  is the interpolation matrix with elements  $\xi_{ij}$ , and  $\underline{q}_f$  and  $\underline{q}_c$  are the vectors containing the nodal values of the parameter  $q$  in the fine and coarse meshing, respectively. Note that the single-grid scheme can be considered as a special case of dual-grid scheme, and  $\Xi$  becomes the identity matrix.

Elements of the Jacobian matrix  $J_c$  for such a problem are defined as  $\frac{\partial M_k}{\partial q_{c_j}}$  (where  $M_k$  is the  $k$ th measurement, and  $q_{c_j}$  is the nodal value of the optical parameter at  $j$ th node of the coarse-grid):

$$J_{c_{kj}} = \frac{\partial M_k}{\partial q_{c_j}} = \sum_{i=1}^{N_f} \frac{\partial M_k}{\partial q_{f_i}} \frac{\partial q_{f_i}}{\partial q_{c_j}}. \quad (20)$$

For the two-step scheme,  $M$  could correspond to internal AOED data, while for the one-step scheme, it could correspond to the boundary PA measurement data. Using Eqs. (18) and (19), we have

$$J_{c_{kj}} = \sum_{i=1}^{N_f} \frac{\partial M_k}{\partial q_{f_i}} \xi_{ij} \Rightarrow J_c = J_f \Xi, \quad (21)$$

where  $J_f$  is the Jacobian matrix computed for the fine-grid.

## 4. NUMERICAL EXPERIMENTS

We have considered a 2 cm × 2 cm domain for fluorescent-light propagation modelling using Eq. (1). This domain is embedded in a 3 cm × 3 cm domain for PA modelling, as indicated in Fig. 3. This configuration is analogous to the physical situation, where tissue is immersed in a water tank, as is common practice for laboratory PA measurements [13,20,24]. In the full data setting, a total of 160 ultrasonic detectors, separated by 1/16 cm (approximately the same as [26]), are arranged on all four sides of a rectangle encompassing the FOT domain, and PA pressure fields were computed by solving the coupled PA-optical Eqs. (1)–(5) in finite element framework for 100 equispaced frequencies between 9.6 and 960 kHz, while, in the limited data setting, the PA signals were computed

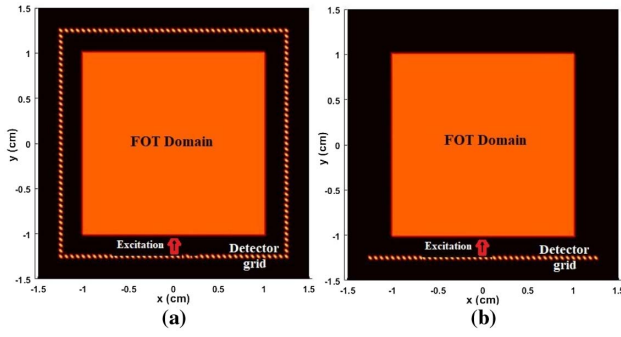


**Fig. 3.** Setup for computational experiments in (a) full and (b) limited data setting.

at 41 detectors placed on the same side as the excitation source as indicated in Fig. 3.

#### Algorithm 1. Two-step dual-grid FPAT algorithm

```

1: procedure TWO-STEP DUAL-GRID FPAT RECONSTRUCTION
2:    $\mu_{axf_c} = \text{zeroes}(N_c \times 1)$ 
3:   Compute  $\Xi$ 
4:    $\mu_{axf_f} \leftarrow \Xi \mu_{axf_c}$ 
5:   Predict synthetic absorbed optical energy density on fine-grid  $\hat{h}_f$ 
6:   Compute PAT measurement matrix  $J_b$ 
7:   Predict boundary PA data  $\underline{p}_f^s$ 
8:   Compute  $\lambda$  using L-curve
9:   Compute the update  $\Delta \hat{h}$ 
10:  PA reconstruction:  $\hat{h}_f^s = \hat{h}_f + \Delta \hat{h}$ 
11:  Compute  $\epsilon \leftarrow \|\hat{h}_f - \hat{h}_f^s\|_2^2$ 
12:  while  $\epsilon \leq \text{tol}$  or the residual is unchanging do
13:     $\mu_{axf_c} \leftarrow \mu_{axf_c}$ 
14:     $\mu_{axf_f} \leftarrow \Xi \mu_{axf_c}$ 
15:    Compute FOT Jacobian on fine-grid  $J_{\mu_f}$ 
16:     $J_{\mu_c} = J_{\mu_f} \Xi$ 
17:    Compute the GN update  $\Delta \mu_{axf_c}$ 
18:    Compute step-length  $\alpha$  using line search
19:     $\mu_{axf_c} \leftarrow \mu_{axf_c} + \alpha \Delta \mu_{axf_c}$ 
20:     $\mu_{axf_f} \leftarrow \Xi \mu_{axf_c}$ 
21:    Predict AOED on fine-grid  $\hat{h}_f$ 
22:    Compute  $\epsilon \leftarrow \|\hat{h}_f - \hat{h}_f^s\|_2^2$ 
23:  end while
24:  return  $\mu_{axf_c}$ 
25: end procedure

```

We note that our Algorithms 1 and 2 are frequency-domain model-based ones, and the choice of frequencies depends upon frequency content in the pressure measurements being considered. In the test cases considered by us, we chose phantom parameters as in [30]; effectively, the maximum frequency present in the photoacoustic measured signal from the phantoms considered was found to be around 1 MHz. Hence, we chose frequencies till around that figure.

We would like to point out that earlier works carried out by the group of Dr. Huabei Jiang utilize 50 frequencies from 50 up to 540 kHz to carry out QPAT reconstructions [38–40]. More recent works by this group [41,42] utilize a transducer with

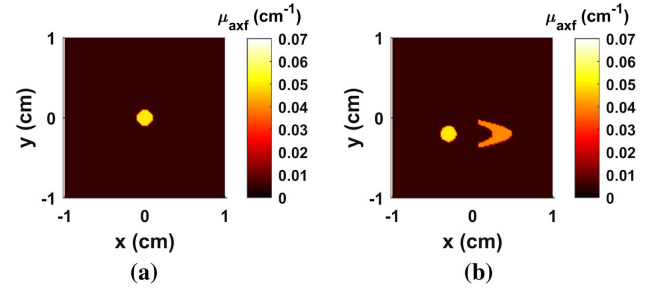


**Fig. 4.** True maps of  $\mu_{axf}$  (a) phantom 1 and (b) phantom 2.

1 MHz central frequency and bandwidth range from 0.65 to 1.18 MHz in multispectral QPAT reconstructions.

The background optical parameters inside the FOT domain were chosen to be  $\mu_{axi} = 0.023 \text{ cm}^{-1}$ ,  $\mu_{ami} = 1.2565 \cdot \mu_{axi}$ ,  $\mu'_{sx} = 9.84 \text{ cm}^{-1}$ ,  $\mu'_{sm} = \mu'_{sx}$ ,  $\phi = 0.4$ ,  $R_{x,m} = 0.431$ ,  $\mu_{axf} = 0.005 \text{ cm}^{-1}$ , and  $\mu_{amf} = 0.1012 \cdot \mu_{axf}$  [30,31]. The two numerical phantoms used in this work are: (i) **phantom 1**: a circular fluorescent target ( $\mu_{axf} = 0.05 \text{ cm}^{-1}$ ) [Fig. 4(a)] and (ii) **phantom 2**: two fluorescent targets; one concave shaped ( $\mu_{axf} = 0.04 \text{ cm}^{-1}$ ) and one circular ( $\mu_{axf} = 0.05 \text{ cm}^{-1}$ ) [Fig. 4(b)]. The homogeneous acoustic properties were chosen to be  $\beta = 4 \times 10^{-4} \text{ K}^{-1}$  and  $C_p = 4000 \text{ J Kg}^{-1} \text{ K}^{-1}$  [24]. In the present work, we only focus on reconstruction of  $\mu_{axf}$ , assuming other parameters to be known.

The synthetic experimental PA data have been generated using a finite element mesh resolution of 1/128 cm. In order not to commit an inverse crime, the iterative forward data have been predicted using a coarser mesh with 1/64 cm resolution. The single- and dual-grid reconstructions have been performed on a mesh with 1/64 and 1/32 cm resolutions, respectively.

#### Algorithm 2. One-step dual-grid FPAT algorithm

```

1: procedure ONE STEP DUAL-GRID FPAT RECONSTRUCTION
2:    $\mu_{axf_c} = \text{zeroes}(N_c \times 1)$ 
3:   Compute  $\Xi$ 
4:    $\mu_{axf_f} \leftarrow \Xi \mu_{axf_c}$ 
5:   Predict absorbed optical energy density on fine-grid  $\hat{h}_f$ 
6:   Compute PAT measurement matrix  $J_b$ 
7:   Predict boundary PA data  $\underline{p}_f^s$ 
8:   Compute  $\epsilon \leftarrow \|\underline{p}^o - \underline{p}_f^s\|_2^2$ 
9:   while  $\epsilon \leq \text{tol}$  or the residual is unchanging do
10:     $\mu_{axf_c} \leftarrow \mu_{axf_c}$ 
11:     $\mu_{axf_f} \leftarrow \Xi \mu_{axf_c}$ 
12:    Compute FOT Jacobian on fine-grid  $J_{\mu_f}$ 
13:     $J = J_b J_{\mu_f}$ 
14:     $J_c = J \Xi$ 
15:    Compute  $\alpha$  using L-curve
16:    Compute the LM update  $\Delta \mu_{axf_c}$ 
17:    Compute step-length  $\alpha$  using line search
18:     $\mu_{axf_c} \leftarrow \mu_{axf_c} + \alpha \Delta \mu_{axf_c}$ 
19:     $\mu_{axf_f} \leftarrow \Xi \mu_{axf_c}$ 
20:    Predict absorbed optical energy density on fine-grid  $\hat{h}_f$ 
21:    Predict boundary PA data  $\underline{p}_f^s$ 
22:    Compute  $\epsilon \leftarrow \|\underline{p}^o - \underline{p}_f^s\|_2^2$ 
23:  end while
24:  return  $\mu_{axf_c}$ 
25: end procedure

```

## 5. RESULTS AND DISCUSSION

The initial guess for  $\mu_{axf}$  has been chosen to be uniformly zero in the domain of interest, and the corresponding AOED map was taken to be the initial guess for  $h$ . The reconstructions have been carried out as proposed in Section 3. The single- and dual-grid reconstructions were carried out at resolutions of 1/64 cm (at 16641 nodes) and 1/32 cm (4225 nodes), respectively, for both full and limited-data settings. The results thus obtained have been shown in terms of reconstructed object images (Figs. 5 and 6 display reconstructions corresponding to single-grid with full data, and dual-grid with limited-data, respectively) as well as error measures obtained (Tables 2 and 3). Laplacian regularized reconstruction results are tabulated in Table 2.

For noiseless data, we observe that both the two-step as well as the one-step algorithms are able to reconstruct the

inhomogeneities well, in all cases (i.e., single- and dual-grid as well as full and limited-data settings). Both the algorithms provide equally good reconstructions with minimal artifacts in the full data setting. However, in the limited data setting, while the two-step algorithm yields spurious-reconstructions (artifacts) in the domain, such artifacts are much fewer in the one-step reconstructions. When the forward data are noisy, the artifacts present in the two-step reconstructions become even more discernible, while the one-step algorithm still provides superior reconstructions. We have observed that single- and dual-grid schemes yield comparable results in both full and limited data settings, thus making it computationally advantageous to use the dual-grid framework.

Accuracy of the reconstructions has been quantified on the basis of the *correlation coefficient* ( $\rho$ ) and the *deviation factor* ( $\delta$ ) defined as [33]

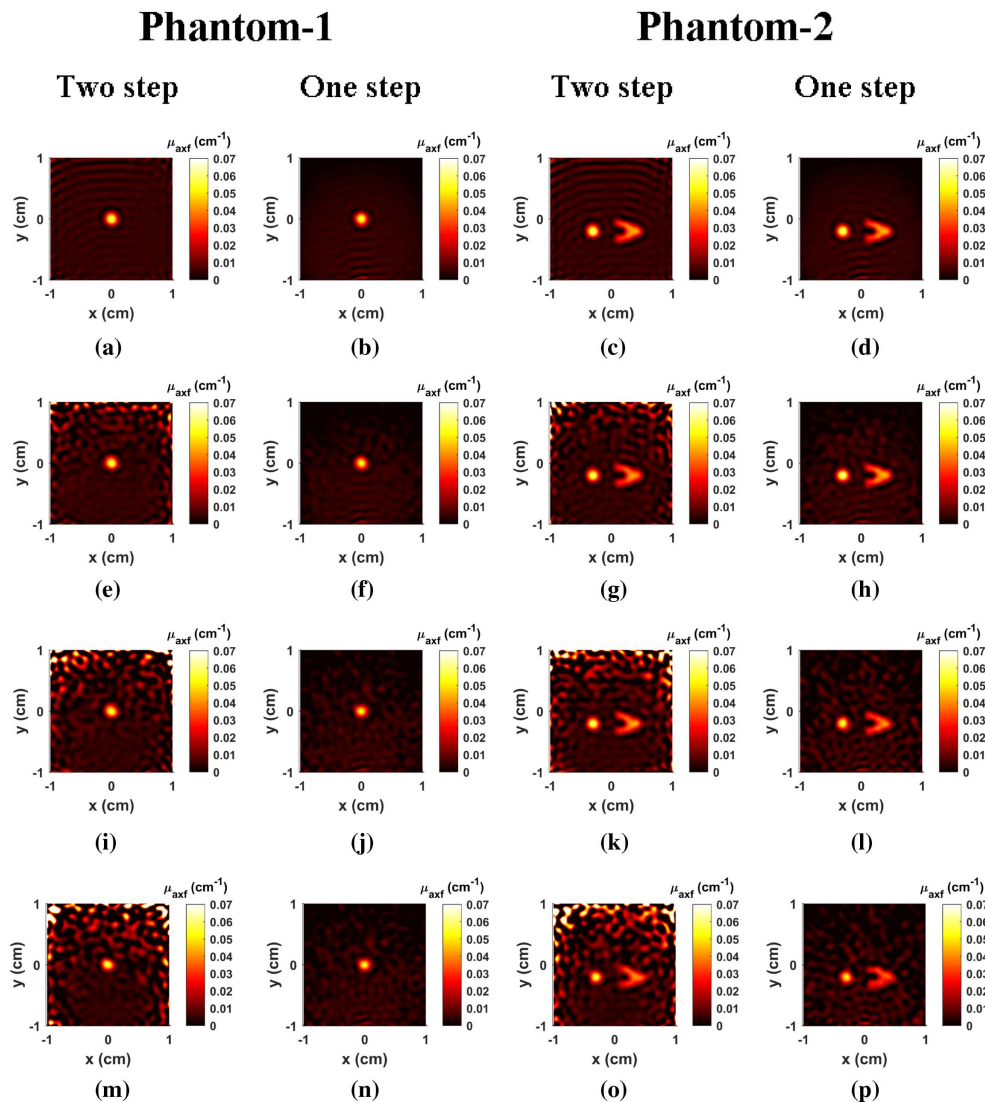


**Fig. 5.** Single-grid reconstructions under full data setting. The first and second columns depict the reconstructions obtained from two- and one-step algorithms, respectively, carried out with (a) and (b) noiseless, (e) and (f) 15 dB SNR, (i) and (j) 10 dB SNR, and (m) and (n) 5 dB SNR PA measurements. The third and fourth columns depict the two- and one-step reconstructions of phantom-2, respectively, carried out with (c) and (d) noiseless, (g) and (h) 15 dB SNR, (k) and (l) 10 dB SNR, (o) and (p) 5 dB SNR PA measurements.

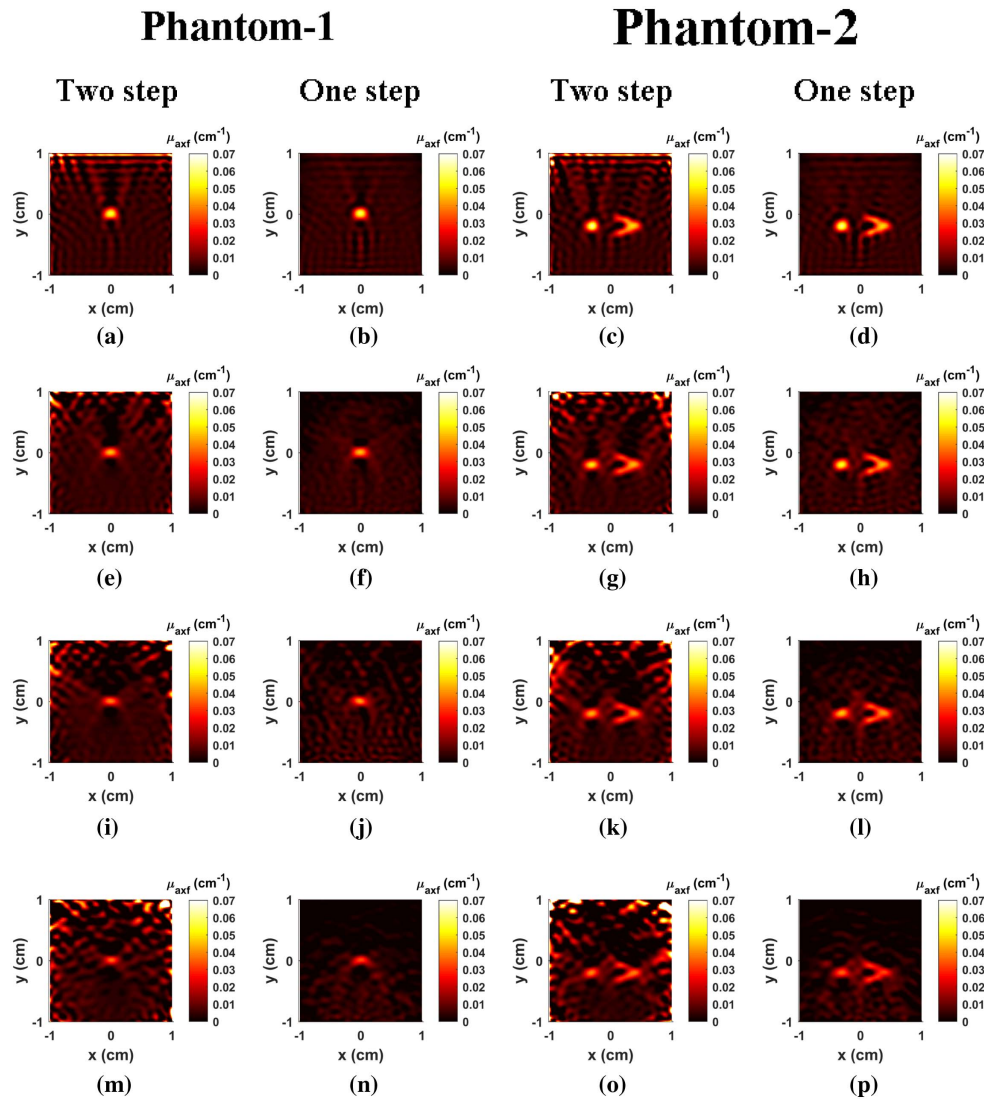


**Fig. 6.** Dual-grid reconstructions under limited data setting. The first and second columns depict the reconstructions obtained from two- and one-step algorithms, respectively, carried out with (a) and (b) noiseless, (e) and (f) 30 dB SNR, (i) and (j) 20 dB SNR, and (m) and (n) 10 dB SNR PA measurements. The third and fourth columns depict the two- and one-step reconstructions of phantom-2, respectively, carried out with (c) and (d) noiseless, (g) and (h) 30 dB SNR, (k) and (l) 20 dB SNR, and (o) and (p) 10 dB SNR PA measurements.

$$\rho = \frac{\sum_{i=1}^N (p_i^r - \bar{p}^r)(p_i^t - \bar{p}^t)}{(N-1)\Delta p^r \Delta p^t};$$

$$\delta = \frac{\sqrt{\sum_{i=1}^N (p_i^r - \bar{p}^r)^2 / N}}{\Delta p^t}, \quad (22)$$

where  $N$  is the total number of nodes,  $\Delta p^r$  and  $\Delta p^t$  are the standard deviations, and  $\bar{p}^r$  and  $\bar{p}^t$  are the mean values of the true and reconstructed values of the parameter, respectively. The values of these accuracy parameters  $\rho$  and  $\delta$  for the reconstruction carried out are tabulated in Tables 2 and 3.

The artifacts in the two-step reconstructions lead to lower correlation coefficients ( $\rho$ ) and higher deviation factors ( $\delta$ ) as compared with the one-step reconstructions. For noisy data, the reconstructed values of the artifacts become significantly higher as compared with the background; as a result, low  $\rho$  and high  $\delta$  values are obtained. The observed ( $\rho$ ,  $\delta$ ) values

justify the claim that the one-step FPAT algorithm is more beneficial as compared with the two-step algorithm. It can also be noticed that the single- and dual-grid one-step reconstructions yield similar  $\rho$  and  $\delta$  values in both full as well as limited data settings. These observations emphasize the utility of going for the dual-grid reconstructions.

The one-step algorithm is able to accurately reconstruct the inhomogeneities for noiseless PA measurements acquired under full as well as limited data settings; hence, corresponding  $\rho$ ,  $\delta$  values are also similar. For noisy data, the one-step algorithm accurately reconstructs the inhomogeneities for the full data settings; therefore, the  $\rho$ ,  $\delta$  values for data sets with SNRs even up to 10 dB are close to their noiseless counterparts.

Under limited data settings, the one- and two-step algorithms are able to recover the location of the inhomogeneities; the shapes and the reconstructed values are recovered accurately



**Table 2. Correlation Coefficients  $\rho$  and Deviation Factors  $\delta$  for the Reconstruction Obtained from Full Data Setting**

Mesh Scheme	Phantom	SNR	One-Step		Two-Step	
			$\rho$	$\delta$	$\rho$	$\delta$
Single-grid	Phantom-1	Noiseless	0.82	0.74	0.83	0.59
		15 dB	0.78	0.87	0.43	1.58
		10 dB	0.74	0.90	0.18	3.96
		5 dB	0.67	0.97	0.15	4.21
	Phantom-2	Noiseless	0.87	0.57	0.84	0.55
		15 dB	0.85	0.63	0.38	1.77
		10 dB	0.81	0.68	0.27	2.48
		5 dB	0.77	0.74	0.17	3.40
Dual-grid	Phantom-1	Noiseless	0.82	0.65	0.80	0.61
		15 dB	0.78	0.81	0.32	2.12
		10 dB	0.74	0.89	0.17	3.84
		5 dB	0.68	0.95	0.14	4.32
	Phantom-2	Noiseless	0.87	0.54	0.83	0.58
		15 dB	0.85	0.62	0.33	2.23
		10 dB	0.79	0.68	0.25	2.63
		5 dB	0.67	0.87	0.09	6.73

enough for data with noise levels up to typically 30 dB in our studies. While the artifacts in the two-step background reconstructions are significantly higher than those in the one-step ones in both full- and limited-data settings, the shapes and optical parameter values are much better reconstructed with full data.

Further, in order to investigate the results with an alternate regularization scheme, dual-grid reconstructions under limited data settings have also been carried out by regularizing the LM scheme [43,44]. At each iterate, the update is computed by solving

$$(\mathbf{J}^T \mathbf{J} + \eta \mathbf{L}^T \mathbf{L}) \Delta \mathbf{q} = -\mathbf{J}^T \mathbf{f}, \quad (23)$$

where  $\mathbf{J}$ ,  $\eta$ ,  $\Delta \mathbf{q}$ , and  $\mathbf{f}$  denote the Jacobian matrix, regularization parameter, update, and the residual of the problem.  $\mathbf{L}^T \mathbf{L}$  denotes the Laplacian matrix, as defined in [35]. The  $\rho$  and  $\delta$  parameters for the Laplacian regularized reconstructions are tabulated in Table 4, and the quality of one-step reconstructions is superior to that of the two-step reconstructions. The Laplacian regularized LM scheme also shows artifacts in the two-step reconstructions. For the one-step FPAT algorithm, the Laplacian regularized LM scheme yielded similar results, as compared with the basic LM scheme for noiseless data.

Thus, we have observed that the one-step method is found to yield superior reconstructions to the two-step one across a wide range of test scenarios. This might be explained by the need of the two-step scheme for an accurate PA reconstruction of the absorbed optical energy density (AOED) from the pressure measurements in order to yield accurate results in the second step (as also mentioned in [20]); the errors of the first step thus cascade into the second. The PA reconstruction problem is an ill-posed one; in addition, under limited data settings PA reconstructions carry more artifacts. In addition, we note that the optical excitation in our work is at the center of the  $y = -1$  cm face (Fig. 3). Deeper inside the domain (with respect to the optical source), where the artifacts in the final two-step reconstruction are seen, we see that the (intermediate) heat source  $\hat{h}$  values are fundamentally lower, thus being susceptible to reconstruction errors and hence increasing the sensitivity of the subsequent second-step reconstruction to noisy effects.

Consequently, the  $\mu_{axf}$  reconstructions thus obtained from the two-step algorithm are more erroneous than the one-step ones. We have observed that, while the one- and two-step schemes yield similar reconstruction quality for noiseless data in full-data settings, as the noise levels increase, as well as in limited-data cases, the one-step scheme outperforms the two-step one.

We have also performed second-step FPAT  $\mu_{axf}$  reconstructions with synthetic internal AOED data perturbed with random noise in the manner of Ren and Zhao [10]. The reconstructions obtained were good in those cases; we obtained  $(\rho, \delta)$  as (0.99,0.07) and (0.98,0.17) for data sets with 2% and 8% noise levels, respectively. This further underlines the

**Table 3. Correlation Coefficients  $\rho$  and Deviation Factors  $\delta$  for the Reconstruction Obtained from Limited Data Setting**

Mesh Scheme	Phantom	SNR	One-Step		Two-Step	
			$\rho$	$\delta$	$\rho$	$\delta$
Single-grid	Phantom-1	Noiseless	0.80	0.63	0.37	1.85
		30 dB	0.70	0.78	0.31	1.74
		20 dB	0.57	1.02	0.25	1.79
		10 dB	0.49	1.18	0.11	3.15
	Phantom-2	Noiseless	0.85	0.54	0.50	1.37
		30 dB	0.82	0.61	0.38	1.62
		20 dB	0.75	0.74	0.30	1.79
		10 dB	0.71	0.87	0.14	3.14
Dual-grid	Phantom-1	Noiseless	0.79	0.64	0.33	1.97
		30 dB	0.68	0.81	0.27	1.88
		20 dB	0.53	1.02	0.22	1.84
		10 dB	0.54	1.14	0.10	3.23
	Phantom-2	Noiseless	0.85	0.55	0.46	1.55
		30 dB	0.81	0.62	0.34	1.85
		20 dB	0.76	0.74	0.29	1.91
		10 dB	0.71	0.86	0.14	3.34

**Table 4. Correlation Coefficients  $\rho$  and Deviation Factors  $\delta$  for the Laplacian Regularized Reconstructions Obtained from Limited Data Setting**

Mesh Scheme	Phantom	SNR	One-Step		Two-Step	
			$\rho$	$\delta$	$\rho$	$\delta$
Dual-grid	Phantom-1	Noiseless	0.83	0.57	0.36	1.82
		30 dB	0.74	0.67	0.31	1.64
		20 dB	0.69	0.72	0.19	2.13
		10 dB	0.47	1.01	0.09	3.52
	Phantom-2	Noiseless	0.87	0.49	0.50	1.40
		30 dB	0.80	0.61	0.41	1.51
		20 dB	0.74	0.70	0.31	1.81
		10 dB	0.63	0.82	0.12	3.29

necessity of incorporation of the first PA step's reconstruction noise (errors) while analyzing the two-step algorithm.

## 6. CONCLUSION

In QPAT reconstructions, it has been reported in the literature that one-step reconstructions of optical properties from boundary PA data perform better than two-step ones that obtain optical properties from the mezzanine reconstruction of the AOED in the entire domain. The utility of a one-step scheme importantly extends to an effective use of dual-representations of field (optical and pressure) variables and optical parameters, which are especially useful in the limited data settings and which effectively helps in constraining optimization search space. To the best of our knowledge, until now there are no comparative reconstruction studies in FPAT with respect to the one- and two-step schemes.

We have demonstrated one- and two-step reconstructions of the fluorophore absorption coefficient in an FPAT framework. We observe that the efficacy of a one-step algorithm is superior to the two-step algorithm in full as well as in limited data settings. The quality of the computationally efficient dual-grid reconstructions is similar to the single-grid reconstructions as also indicated by the correlation and deviation errors, thus making use of dual-grid schemes computationally advantageous. It is also observed that, for the full data setting, the one- and two-step schemes are able to quantitatively recover the inhomogeneities for PA data with SNR as low as 10 dB; in the limited data setting, the shapes and quantitative values are accurately reconstructed from PA data of typically up to 30 dB SNR.

## APPENDIX A: FINITE ELEMENT FORMULATION OF COUPLED DIFFUSION EQUATIONS

In this section, for the sake of clarity, we have briefly outlined the formulation of the CDE in Eq. (1) as given in [25]. The field variables approximated using linear basis functions are expressed as

$$\Phi_x \approx \hat{\Phi}_x = \mathbf{N}\underline{\phi}_x; \quad \Phi_m \approx \hat{\Phi}_m = \mathbf{N}\underline{\phi}_m. \quad (\text{A1})$$

Weighted residual forms of the governing Eq. (1) using the Galerkin finite element method are

$$\begin{aligned} \int_{\Omega} [\mathbf{N}]^T (-\nabla \cdot (D_x \nabla \hat{\Phi}_x) + k_x \hat{\Phi}_x) &= \int_{\Omega} [\mathbf{N}]^T S_x \\ \int_{\Omega} [\mathbf{N}]^T (-\nabla \cdot (D_m \nabla \hat{\Phi}_m) + k_m \hat{\Phi}_m) &= \int_{\Omega} [\mathbf{N}]^T \beta \hat{\Phi}_x. \end{aligned} \quad (\text{A2})$$

In order to model the 2D domain, linear triangular elements have been used, and the nodal basis for an element is  $[\mathbf{N}] = [N_1 \ N_2 \ N_3]$ . The point source of strength  $Q$  is  $S_x := Q \cdot \delta(\vec{r} - \vec{r}_s)$ , where  $\vec{r}_s$  is located at a depth of  $1/(\mu_{axi} + \mu'_{ix})$  (one mean free path) [45]. Define the following kernels:

$$\begin{aligned} \mathbf{K}_s &= \left[ \int_{\Omega_e} (\nabla[\mathbf{N}])^T \nabla[\mathbf{N}] \right], \quad \mathbf{K}_m = \left[ \int_{\Omega_e} [\mathbf{N}]^T [\mathbf{N}] \right], \\ \mathbf{K}_b &= \left[ \int_{\partial\Omega_e} [\mathbf{N}]^T [\mathbf{N}] \right]. \end{aligned} \quad (\text{A3})$$

For one element, the matrix form of Eq. (A2) is written as

$$\mathbf{A}_x \underline{\phi}_x = \underline{\varepsilon}_x; \quad \mathbf{A}_m \underline{\phi}_m = \mathbf{M}_\beta \underline{\phi}_x, \quad (\text{A4})$$

where,  $\underline{\varepsilon}_x = \int_{\Omega} [\mathbf{N}]^T S_x = Q[N_1(\vec{r}_s)N_2(\vec{r}_s)N_3(\vec{r}_s)]^T$ ,  $\mathbf{A}_x = \mathcal{A}(D_x, k_x, b_x)$ ,  $\mathbf{A}_m = \mathcal{A}(D_m, k_m, b_m)$ ,  $\mathbf{M}_\beta = \mathcal{M}(\beta)$ , and

$$\mathcal{A}(D, k, b) = \mathbf{K}_s D + \mathbf{K}_m k + \mathbf{K}_b b; \quad \mathcal{M}(\beta) = \mathbf{K}_m \beta. \quad (\text{A5})$$

$[\mathbf{A}_x]$ ,  $[\mathbf{A}_m]$ , and  $[\mathbf{M}_\beta]$  are the assembled matrices of  $[A_x]$ ,  $[A_m]$ , and  $[M_\beta]$ , respectively, for all elements. The block form of the matrix equations, which need to be solved to obtain the forward solution, is

$$\begin{bmatrix} \mathbf{A}_x & \mathbf{0} \\ -\mathbf{M}_\beta & \mathbf{A}_m \end{bmatrix} \begin{bmatrix} \underline{\phi}_x \\ \underline{\phi}_m \end{bmatrix} = \begin{bmatrix} \underline{\varepsilon}_x \\ \underline{0} \end{bmatrix}. \quad (\text{A6})$$

The discretized heat source for a nominal distribution of the fluorophore absorption coefficient  $\underline{\mu}_{axf}$  is given by

$$\underline{h} \equiv \mathcal{H}(\underline{\mu}_{axf}) = (\underline{\mu}_{axi} + \underline{\mu}_{axf}) \odot \underline{\phi}_x + (\underline{\mu}_{ami} + \underline{\mu}_{amf}) \odot \underline{\phi}_m, \quad (\text{A7})$$

where  $\mathcal{H}$  denotes the heat source operator,  $\odot$  represents the pointwise multiplication, and  $\underline{\phi}_x$  and  $\underline{\phi}_m$  are obtained by solving Eq. (A6).

## APPENDIX B: FINITE ELEMENT FORMULATION OF PHOTOACOUSTIC EQUATION

In this section, we briefly review the finite element formulation of the PA Eq. (4) as detailed in [27,46]. The complex PA field variables approximated using linear basis functions are expressed as

$$p \approx \hat{p} = \mathbf{N}\underline{p}; \quad h \approx \hat{h} = \mathbf{N}\underline{h}. \quad (\text{B1})$$

The weighted residual forms of Eq. (4) using Galerkin formulation are

$$\int_{\Omega} [\mathbf{N}]^T (\nabla^2 + k^2) \hat{p} = \int_{\Omega} [\mathbf{N}]^T i k \frac{v\beta}{C_p} \hat{h}. \quad (\text{B2})$$

The matrix form of the equations for  $j$ th frequency is given by [27]

$$\mathbf{A}^j \underline{p} = \mathbf{B}^j \underline{h} \quad (\text{B3})$$

where,

$$\mathbf{A}^j = -\mathbf{K}_s + k_j^2 \mathbf{K}_m + -i k_j \mathbf{K}_b; \quad \mathbf{B}^j = i k_j \frac{v\beta}{C_p} \mathbf{K}_m. \quad (\text{B4})$$

The kernels  $\mathbf{K}_s$ ,  $\mathbf{K}_m$ , and  $\mathbf{K}_b$  are defined in Eq. (A3), and  $k_j$  denotes the wavenumber corresponding to the  $j$ th frequency.

## APPENDIX C: PAT MEASUREMENT MATRIX

The complex PA measurement  $\underline{p}_{\text{comp}}^j$  on  $M$  detector nodes can be expressed as

$$\underline{p}_{\text{comp}}^j = \mathcal{D} \underline{p} = \mathcal{D}(\mathbf{A}^j)^{-1} \mathbf{B}^j \underline{h} = \mathbf{J}^j \underline{h}, \quad (\text{C1})$$

where  $\mathcal{D}$  is the binary detection matrix operator of size  $M \times N$ , and  $\mathbf{J}^j$  is the complex measurement operator for the  $j$ th frequency. Each row of  $\mathcal{D}$  is constructed of  $N$  elements, where all but one element corresponding to the detector node number are zero.

The measurement operator  $J_b$  is written as

$$J_b = [[\text{Re}\{\mathcal{J}\}]^T, [\text{Im}\{\mathcal{J}\}]^T]^T, \quad (\text{C2})$$

where  $\mathcal{J} = [\mathcal{J}^1]^T, [\mathcal{J}^2]^T, \dots, [\mathcal{J}^L]^T]^T$  and the complete PA measurement equation can be expressed as the linear system

$$\underline{p}_{\text{meas}} = J_b \underline{b}. \quad (\text{C3})$$

Combining Eqs. (A7) and (C3), the discrete FPAT measurement equation can be written as

$$\underline{p}_{\text{meas}} \equiv J_b \mathcal{H}(\underline{\mu}_{\text{axf}}) \equiv \mathcal{G}(\underline{\mu}_{\text{axf}}), \quad (\text{C4})$$

where  $\mathcal{G} = J_b \mathcal{H}$  is the discrete measurement operator, with  $\mathcal{H}$  being defined in Eq. (A7).

**Acknowledgment.** We thank the anonymous reviewers for their comments, which have helped us to improve the manuscript. PKP acknowledges the support of CSIR and BRNS India during parts of the work.

## REFERENCES

1. A. Corlu, R. Choe, T. Durduran, M. A. Rosen, M. Schweiger, S. R. Arridge, M. D. Schnall, and A. G. Yodh, "Three-dimensional in vivo fluorescence diffuse optical tomography of breast cancer in humans," *Opt. Express* **15**, 6696–6716 (2007).
2. H. Egger, M. Freiberger, and M. Schlottbom, "On forward and inverse models in fluorescence diffuse optical tomography," *Inverse Probl. Imaging* **4**, 411–427 (2010).
3. G. Ku and L. V. Wang, "Deeply penetrating photoacoustic tomography in biological tissues enhanced with an optical contrast agent," *Opt. Lett.* **30**, 507–509 (2005).
4. J. Koo, M. Jeon, Y. Oh, H. W. Kang, J. Kim, C. Kim, and J. Oh, "In vivo non-ionizing photoacoustic mapping of sentinel lymph nodes and bladders with ICG-enhanced carbon nanotubes," *Phys. Med. Biol.* **57**, 7853–7862 (2012).
5. D. Yang, H. Wang, C. Sun, H. Zhao, K. Hu, W. Qin, R. Ma, F. Yin, X. Qin, Q. Zhang, Y. Liang, and Z. Li, "Development of a high quantum yield dye for tumour imaging," *Chem. Sci.* **8**, 6322–6326 (2017).
6. V. Ntziachristos, J. Ripoll, L. V. Wang, and R. Weissleder, "Looking and listening to light: the evolution of whole-body photonic imaging," *Nat. Biotechnol.* **23**, 313–320 (2005).
7. F. Stuker, J. Ripoll, and M. Rudin, "Fluorescence molecular tomography: principles and potential for pharmaceutical research," *Pharmaceutics* **3**, 229–274 (2011).
8. L. Hervé, A. Koenig, and J. Dinten, "Non-uniqueness in fluorescence-enhanced continuous wave diffuse optical tomography," *J. Opt.* **13**, 015702 (2011).
9. F. Leblond, H. Dehghani, D. Kepshire, and B. W. Pogue, "Early-photon fluorescence tomography: spatial resolution improvements and noise stability considerations," *J. Opt. Soc. Am. A* **26**, 1444–1457 (2009).
10. K. Ren and H. Zhao, "Quantitative fluorescence photoacoustic tomography," *SIAM J. Imaging Sci.* **6**, 2404–2429 (2013).
11. K. Ren, R. Zhang, and Y. Zhong, "Inverse transport problems in quantitative pat for molecular imaging," *Inverse Probl.* **31**, 125012 (2015).
12. C. Wang and T. Zhou, "A hybrid reconstruction approach for absorption coefficient by fluorescence photoacoustic tomography," arXiv:1806.07086 (2018).
13. D. Razansky and V. Ntziachristos, "Hybrid photoacoustic fluorescence molecular tomography using finite-element-based inversion," *Med. Phys.* **34**, 4293–4301 (2007).
14. Z. Yuan and H. Jiang, "Quantitative photoacoustic tomography: Recovery of optical absorption coefficient maps of heterogeneous media," *Appl. Phys. Lett.* **88**, 231101 (2006).
15. B. T. Cox, S. R. Arridge, K. P. Köstli, and P. C. Beard, "Two-dimensional quantitative photoacoustic image reconstruction of absorption distributions in scattering media by use of a simple iterative method," *Appl. Opt.* **45**, 1866–1875 (2006).
16. R. J. Zemp, "Quantitative photoacoustic tomography with multiple optical sources," *Appl. Opt.* **49**, 3566–3572 (2010).
17. G. Bal and K. Ren, "Multi-source quantitative photoacoustic tomography in a diffusive regime," *Inverse Probl.* **27**, 075003 (2011).
18. T. Saratoon, T. Tarvainen, B. Cox, and S. Arridge, "A gradient-based method for quantitative photoacoustic tomography using the radiative transfer equation," *Inverse Probl.* **29**, 075006 (2013).
19. B. Banerjee, S. Bagchi, R. M. Vasu, and D. Roy, "Quantitative photoacoustic tomography from boundary pressure measurements: non-iterative recovery of optical absorption coefficient from the reconstructed absorbed energy map," *J. Opt. Soc. Am. A* **25**, 2347–2356 (2008).
20. Z. Yuan and H. Jiang, "A calibration-free, one-step method for quantitative photoacoustic tomography," *Med. Phys.* **39**, 6895–6899 (2012).
21. M. Venugopal, P. van Es, S. Manohar, D. Roy, and R. M. Vasu, "Quantitative photoacoustic tomography by stochastic search: direct recovery of the optical absorption field," *Opt. Lett.* **41**, 4202–4205 (2016).
22. S. Bagchi, "Studies on quantitative photoacoustic tomography: model-based reconstruction using deterministic and stochastic algorithms," Ph.D. thesis (Indian Institute of Science, 2012).
23. P. K. Pandey, O. Gottam, N. Naik, P. Singh, and A. Pradhan, "One step quantitative fluorescence photoacoustic tomography," in *International Conference on Fibre Optics and Photonics* (OSA, 2016), paper P1A.24.
24. L. V. Wang and H.-I. Wu, *Biomedical Optics: Principles and Imaging*, 1st ed. (Wiley, 2007).
25. F. Fedele, J. Laible, and M. Eppstein, "Coupled complex adjoint sensitivities for frequency-domain fluorescence tomography: theory and vectorized implementation," *J. Comput. Phys.* **187**, 597–619 (2003).
26. M. Xu and L. V. Wang, "Universal back-projection algorithm for photoacoustic computed tomography," *Phys. Rev. E* **71**, 016706 (2005).
27. Y. Sun, "Three-dimensional photoacoustic tomography and its application to detection of joint diseases in the hand," Ph.D. thesis (University of Florida, 2010).
28. S. Bagchi, D. Roy, and R. M. Vasu, "Forward problem solution in photoacoustic tomography by discontinuous Galerkin method," in *Bio-Optics: Design and Application* (OSA, 2011), paper JTuA22.
29. H. Gan, P. Levin, and R. Ludwig, "Finite element formulation of acoustic scattering phenomena with absorbing boundary condition in the frequency domain," *J. Acoust. Soc. Am.* **94**, 1651–1662 (1993).
30. A. Joshi, W. Bangerth, and E. M. Sevick-Muraca, "Adaptive finite element based tomography for fluorescence optical imaging in tissue," *Opt. Express* **12**, 5402–5417 (2004).
31. A. B. Thompson, "Development of a new optical imaging modality for detection of fluorescence-enhanced disease," Ph.D. thesis (Texas A&M University, 2003).
32. R. Zhang, "Hybrid inverse problems in molecular imaging," Ph.D. thesis, University of Texas, Austin, Texas, (2017).
33. A. Klose, "Optical tomography based on the equation of radiative transfer," Ph.D. thesis (Freie Universität Berlin, 2002).
34. P. C. Hansen, "Regularization tools: a MATLAB package for analysis and solution of discrete ill-posed problems," *Numer. Algorithms* **6**, 1–35 (1994).
35. M. Schweiger, S. R. Arridge, and I. Nissilä, "Gauss-newton method for image reconstruction in diffuse optical tomography," *Phys. Med. Biol.* **50**, 2365–2386 (2005).
36. K. D. Paulsen, P. M. Meaney, M. J. Moskowitz, and J. M. Sullivan, "A dual mesh scheme for finite element based reconstruction algorithms," *IEEE Trans. Med. Imag.* **14**, 504–514 (1995).
37. X. Gu, Y. Xu, and H. Jiang, "Mesh-based enhancement schemes in diffuse optical tomography," *Med. Phys.* **30**, 861–869 (2003).
38. Z. Yuan, Q. Wang, and H. Jiang, "Reconstruction of optical absorption coefficient maps of heterogeneous media by photoacoustic tomography coupled with diffusion equation based regularized newton method," *Opt. Express* **15**, 18076–18081 (2007).
39. Z. Yuan and H. Jiang, "Quantitative photoacoustic tomography," *Philos. Trans. R. Soc. A* **367**, 3043–3054 (2009).

40. Z. Yuan and H. Jiang, "Simultaneous recovery of tissue physiological and acoustic properties and the criteria for wavelength selection in multispectral photoacoustic tomography," *Opt. Lett.* **34**, 1714–1716 (2009).
41. Y. Liu, H. Jiang, and Z. Yuan, "Two schemes for quantitative photoacoustic tomography based on Monte Carlo simulation," *Med. Phys.* **43**, 3987–3997 (2016).
42. Y. Liu and Z. Yuan, "Multi-spectral photoacoustic elasticity tomography," *Biomed. Opt. Express* **7**, 3323–3334 (2016).
43. A. Doicu, T. Trautmann, and F. Schreier, *Numerical Regularization for Atmospheric Inverse Problems* (Springer, 2010).
44. N. Naik, N. Patil, Y. Yadav, J. Eriksson, and A. Pradhan, "Fully non-linear  $SP_3$  approximation based fluorescence optical tomography," *IEEE Trans. Med. Imag.* **36**, 2308–2318 (2017).
45. M. Schweiger, S. Arridge, M. Hiraoka, and D. Delpy, "The finite element method for the propagation of light in scattering media: boundary and source conditions," *Med. Phys.* **22**, 1779–1792 (1995).
46. Z. Yuan, H. Zhao, C. Wu, Q. Zhang, and H. Jiang, "Finite-element-based photoacoustic tomography: phantom and chicken bone experiments," *Appl. Opt.* **45**, 3177–3183 (2006).